Higher-Order 3D-Shell Elements and Anisotropic 3D Yield Functions for Improved Sheet Metal Forming Simulations: Part I

Maximilian Schilling[1], Tobias Willmann[1], Alexander Wessel[2,3], Alexander Butz[2], Manfred Bischoff[1]

[1]University of Stuttgart, Institute for Structural Mechanics,
Pfaffenwaldring 7, 70550 Stuttgart, Germany
[2]Fraunhofer Institute for Mechanics of Materials IWM,
Woehlerstrasse 11, 79108 Freiburg, Germany
[3]Technical University of Munich, Chair of Metal Forming and Casting,
Walther-Meissner-Strasse 4, 85748 Garching, Germany

1 Abstract

Sheet metal forming simulations are crucial in various industries, such as automotive, aerospace, and construction. These simulations are commonly carried out using Reissner-Mindlin shell elements, which involve certain simplifying assumptions about zero normal stress in shell normal direction and cross-sectional fibers remaining straight during deformation [1]. Because of this, the material model needs to be modified and no three-dimensional material model can be used. However, in critical forming situations such as bending with small radii relative to the sheet thickness, these assumptions do not hold, resulting in inaccurate simulation results. To address this issue, a higher-order 3D-shell element that incorporates a full three-dimensional constitutive model and that can account for cross-sectional warping and higher-order strain distributions has been developed [2].
First findings on the benefits of using higher-order 3D-shell elements for accurately modeling sheet metal forming processes were presented in [3]. The objective of this study is to expand upon this work by assessing the accuracy of simulations utilizing the higher-order 3D-shell element for critical sheet metal forming processes. Results of simulations with the higher-order 3D-shell elements are compared to experimental data and results obtained from simulations with solid elements and Reissner-Mindlin shell elements. It is demonstrated that simulations with higher-order 3D-shell elements provide more accurate predictions in sheet metal forming processes than the standard modeling approach, including but not limited to stress.
Furthermore, we aim to support the efficient utilization of the higher-order 3D-shell element by identifying situations in which the additional deformation modes of this element are beneficial, and in which application of a standard shell element suffices. To achieve this, we analyze the influence of its higher-order deformation modes on the strain for parameter alterations in benchmark problems. To aid the modeling decision, mesh studies are conducted to quantify the influence of the element size on the results quality. Lastly, a comparison of numerical efficiency of different element formulations is given, showing the high efficiency of higher-order 3D-shell elements compared to solid elements.
This contribution is part one of a two-part series that aims to present recent improvements of sheet metal forming simulations through a combination of higher-order 3D-shell elements and anisotropic 3D yield models. Part I focuses on the assessment of higher-order 3D-shell elements, while Part II investigates the effect of anisotropic 3D yield models with respect to the in-plane and out-of-plane behavior on sheet metal forming simulations. Together, these contributions aim to provide a comprehensive overview of the latest advances obtained in a joint research project at the Fraunhofer IWM in Freiburg and the Institute for Structural Mechanics at the University of Stuttgart.

2 Higher-order 3D-shell elements

Conversely to shell elements currently available in LS-DYNA, the 3D-shell element utilized for the simulations in this contribution allows for quadratic and cubic cross-sectional warping and a higher order strain field with respect to the transverse coordinate. This element is denoted as *cubic 3D-shell element* in the following. Figure 1 illustrates various components of its deformation. More fundamental information on the cubic 3D-shell element can be found in [2]. Several techniques to prevent locking are implemented. Transverse shear locking and curvature-thickness locking are eliminated through the assumed natural strain method [4]. In extension to the element formulation given in [2], in-plane shear locking and in-plane volumetric locking are prevented using reduced integration techniques. While the element formulation from [2] included an incompatible strain field of third order in transverse direction, the element formulation in this contribution is enhanced with an additional incompatible quartic strain

field in transverse direction to prevent nonlinear Poisson stiffening. For more information on this stiffening effect and its prevention the reader is directed to [5].

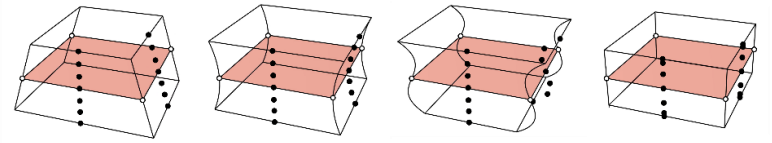

Fig.1: Visualization of the deformation modes of the cubic 3D-shell element including (from left) linear, quadratic, cubic deformations of cross-sectional fibers and a quadratic deformation in transverse direction [3].

In addition to the cubic 3D-shell element, variants with reduced deformation modes were developed. These are a *quadratic 3D-shell element* enhanced with an incompatible cubic strain field in transverse direction and a *linear 3D-shell element* enhanced with an incompatible quadratic strain field in transverse direction. Both elements employ the same element technologies as the cubic 3D-shell element.
To enhance the efficiency of the 3D-shell elements, a different implementation for the calculation of the velocity strain $\mathbf{D}$, also known as the rate of deformation, is used. For the fundamentals, the reader is referred to [6]. There are two variants to express the velocity strain $\mathbf{D}$ based on the contravariant ($\mathbf{g}^i$) and covariant ($\mathbf{g}_i$) base vectors, either by

$$\mathbf{D} = \frac{1}{2}\left(\dot{\mathbf{g}}_i \cdot \mathbf{g}_j + \mathbf{g}_i \cdot \dot{\mathbf{g}}_j\right)\mathbf{g}^i \otimes \mathbf{g}^j \tag{1}$$

or by

$$\mathbf{D} = \frac{1}{2}\left(\dot{\mathbf{g}}_i \otimes \mathbf{g}^i + \mathbf{g}^i \otimes \dot{\mathbf{g}}_i\right). \tag{2}$$

For 3D-shell element, the coefficients D_{ij}^{CO} of the velocity strain with respect to the corotational base vectors ($\hat{\mathbf{e}}^i$) are required

$$\mathbf{D} = D_{ij}^{\mathrm{CO}}\hat{\mathbf{e}}^i \otimes \hat{\mathbf{e}}^j. \tag{3}$$

Choosing Equation (2) allows to calculate the coefficients D_{ij}^{CO} of the velocity strain directly without using any transformation relation but just by insertion of the contravariant base vectors in terms of the corotational base vectors and the time derivative of the covariant base vectors in terms of the corotational base vectors:

$$\mathbf{D} = \frac{1}{2}\left(\dot{\mathbf{g}}_i \otimes \mathbf{g}^i + \mathbf{g}^i \otimes \dot{\mathbf{g}}_i\right) = \frac{1}{2}\left([\dot{g}_k]^i\,\hat{\mathbf{e}}^i \otimes [g^k]^j\,\hat{\mathbf{e}}^j + [g^k]^j\,\hat{\mathbf{e}}^j \otimes [\dot{g}_k]^i\,\hat{\mathbf{e}}^i\right) \tag{4}$$

$$= \underbrace{\frac{1}{2}\left([\dot{g}_k]^i\,[g^k]^j + [g^k]^j\,[\dot{g}_k]^i\right)}_{D_{ij}^{\mathrm{CO}}}\hat{\mathbf{e}}^i \otimes \hat{\mathbf{e}}^j. \tag{5}$$

This results in the following expression for the velocity strain components D_{ij}^{CO} in Voigt notation with respect to the corotational base

$$\overline{\mathbf{D}}^{\mathrm{CO}} = \begin{bmatrix} D_{11}^{\mathrm{CO}} \\ D_{22}^{\mathrm{CO}} \\ D_{33}^{\mathrm{CO}} \\ 2D_{12}^{\mathrm{CO}} \\ 2D_{13}^{\mathrm{CO}} \\ 2D_{23}^{\mathrm{CO}} \end{bmatrix} = \begin{bmatrix} [\dot{g}_1]^1\,[g^1]^1 + [\dot{g}_2]^1\,[g^2]^1 + [\dot{g}_3]^1\,[g^3]^1 \\ [\dot{g}_1]^2\,[g^1]^2 + [\dot{g}_2]^2\,[g^2]^2 + [\dot{g}_3]^2\,[g^3]^2 \\ [\dot{g}_1]^3\,[g^1]^3 + [\dot{g}_2]^3\,[g^2]^3 + [\dot{g}_3]^3\,[g^3]^3 \\ [\dot{g}_1]^1\,[g^1]^2 + [\dot{g}_2]^1\,[g^2]^2 + [\dot{g}_3]^1\,[g^3]^2 + [\dot{g}_1]^2\,[g^1]^1 + [\dot{g}_2]^2\,[g^2]^1 + [\dot{g}_3]^2\,[g^3]^1 \\ [\dot{g}_1]^1\,[g^1]^3 + [\dot{g}_2]^1\,[g^2]^3 + [\dot{g}_3]^1\,[g^3]^3 + [\dot{g}_1]^3\,[g^1]^1 + [\dot{g}_2]^3\,[g^2]^1 + [\dot{g}_3]^3\,[g^3]^1 \\ [\dot{g}_1]^2\,[g^1]^3 + [\dot{g}_2]^2\,[g^2]^3 + [\dot{g}_3]^2\,[g^3]^3 + [\dot{g}_1]^3\,[g^1]^2 + [\dot{g}_2]^3\,[g^2]^2 + [\dot{g}_3]^3\,[g^3]^2 \end{bmatrix}. \tag{6}$$

This calculation method requires considerably fewer arithmetic operations than the previous calculation method using transformation tensors to convert the velocity strain to the corotational base.

3 Improved prediction quality in sheet metal forming processes

Initial benefits of higher order 3D-shell elements for accurate sheet metal forming simulations were reported in [3]. In the following, we extend these findings by evaluating the accuracy of the higher-order 3D-shell element for more sheet metal forming processes. The comparative analysis involves simulations with higher-order 3D-shell elements against experimental data, linear solid elements, and standard Reissner-Mindlin shell elements.

3.1 Hat profile with double draw bead

In numerous sheet metal forming processes, draw beads are employed to regulate material flow into the component form. A draw bead can be defined as an elevated region designed along the die profile, introducing controlled resistance to the sheet metal flow. The sheet metal undergoes sequential bending and unbending around a small radius in the draw bead. This results in a complex stress and strain state due to alternating one-sided contact and the involved friction, and small-radius bending. Regularly, sheet metal forming processes incorporate multiple draw beads to manipulate material flow [7]. This study examines a hat profile, focusing on the equipped double draw bead. The bead geometry closely aligns with those utilized in the automotive sector without corresponding to a specific draw bead profile and was provided by the BMW Group. Figure 2 (left) shows the hat profile and double draw bead geometry, extending infinitely in the Y-direction (plane strain condition). Figure 2 (right) shows a detail of the double draw bead geometry with the deformed blank. For the simulation, an aluminum sheet metal (*`MAT024`= *`MAT_PIECEWISE_LINEAR_PLASTICITY`) with dimensions $370\,\mathrm{mm} \times 5\,\mathrm{mm}$ and a sheet thickness of $T = 1.00\,\mathrm{mm}$ is used. An element size $h = 1.00\,\mathrm{mm}$ is chosen for the XY-plane and nine Gauss points in sheet-thickness direction are used for simulations with shell elements. Correspondingly, nine solid elements in sheet-thickness direction with the same element size h are used. In the simulation, the blank is first clamped between blank holder and hat profile (displacement controlled), then the punch moves in positive Z-direction (displacement controlled) and by this pulls the blank through the draw bead into the hat profile. For reasons of confidentiality, more detailed geometry information on this model cannot be disclosed.

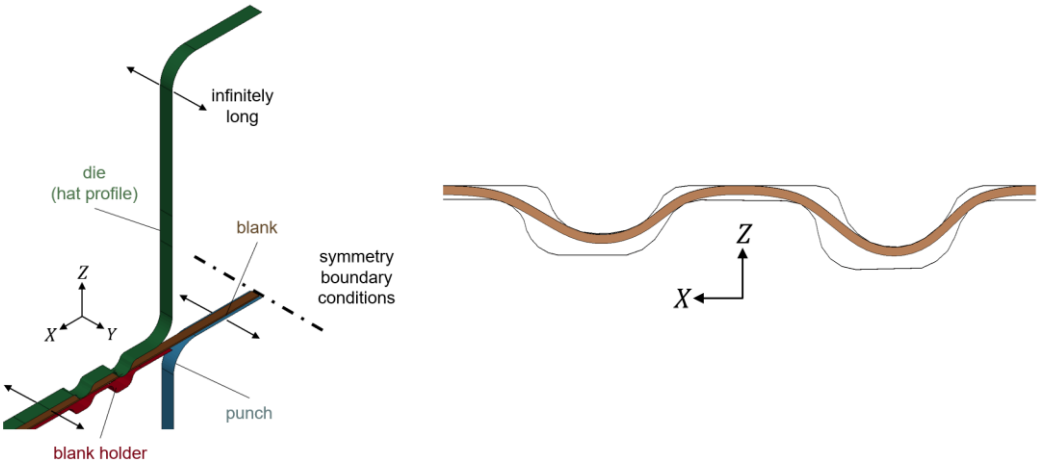

Fig.2: Simulation model for the hat profile with double draw bead (left, geometry provided by BMW Group) and detail of the closed double draw bead with the deformed sheet metal (right).

Selected results with focus on the draw bead are shown in Figure 3 for three different element formulations. Reissner-Mindlin shell elements and cubic 3D-shell elements are compared against a full three-dimensional simulation with nine solid elements across the sheet thickness.

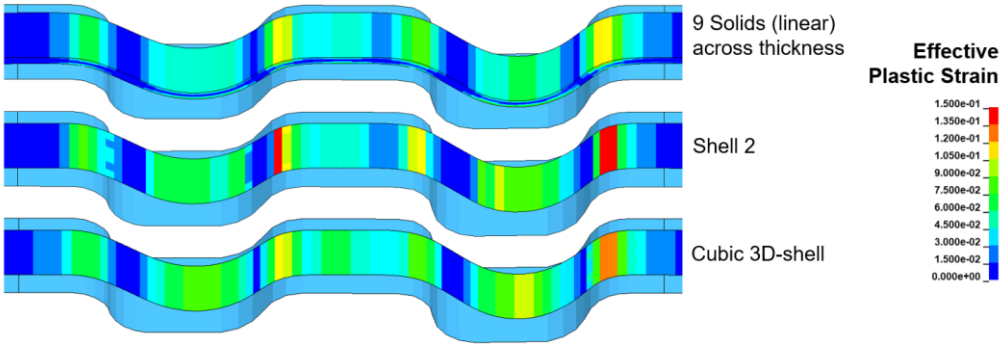

Fig.3: Comparison of effective plastic strain at the upper blank surface in the double draw bead shortly after beginning of deep drawing process for different element formulations.

Figure 3 displays the effective plastic strain at the upper blank surface during the initial stages of the deep drawing process. At this point, the material has only traversed one draw bead. A comparison is made between the standard shell element (Shell 2) and the cubic 3D-shell element, simulations using nine solid elements across the thickness are used as a reference. The results depicted in Figure 3

indicate that Shell 2 tends to overestimate the effective plastic strain, particularly in regions with small bending radii, such as the sharp corners found at the ends of the two draw beads. It is worth noting that this overestimation may become more pronounced in later stages of the simulation when the material has fully traversed both draw beads. In contrast to this, the cubic 3D-shell element exhibits a much closer alignment with the solution obtained using solid elements, particularly in regions with small bending radii.
It is clear that such a difference in results at the draw bead between the standard shell and three-dimensional reference solution has an impact on the outcome of the final part and reduces the results quality. To conduct a more in-depth analysis of the influence of these errors on the predicted final part geometry, implicit spring back analyses are required. However, these types of analyses are not yet implemented for the higher-order 3D-shell element and, therefore, fall outside the scope of this contribution.

3.2 Stretch bending test

A stretch bending test of an aluminum sheet metal strip (AA6014-T4 aluminum alloy) is performed to investigate processes involving simultaneous stretching and bending. The geometry of the stretch bending test is shown in Figure 4. The dimensions of the sheet are $250.0\,\mathrm{mm} \times 25.0\,\mathrm{mm}$, with a thickness of $T = 1.00\,\mathrm{mm}$. For the experiment, the sheet is clamped between a blank holder and a die, with a die radius of $5\,\mathrm{mm}$. The punch with a radius of $5\,\mathrm{mm}$ is located at a distance of $44.5\,\mathrm{mm}$ from the blank holder. The punch was moved in positive Z-direction with displacement control until failure occurred. The simulation model involves an ideal clamp for the sheet (all degrees of freedom fixed), a **`*MAT024`** material model, and different shell element formulations. Additionally, five linear solids are used across the sheet thickness for comparison. For each element formulation a mesh with element length of $h = 0.3\,\mathrm{mm}$ in the XY-plane is used. In the simulation, the punch is also moved with displacement control.

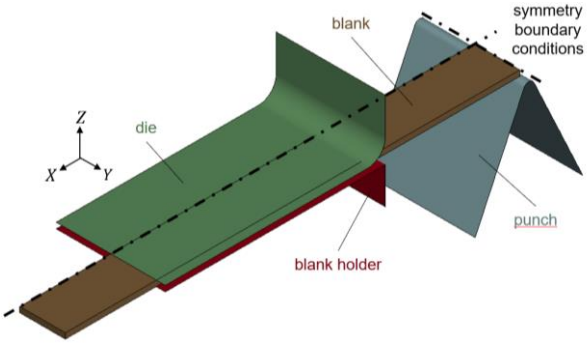

Fig.4: Simulation model for the stretch bending test.

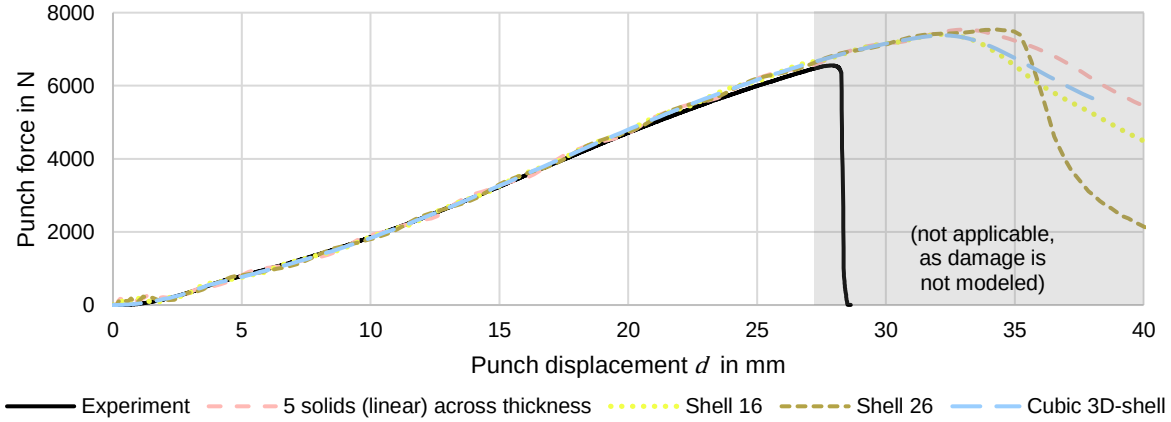

Fig.5: Force-displacement diagram for the stretch bending test.

Figure 5 demonstrates a close alignment among all element formulations (shells and solids) concerning the force-displacement curve of the punch. Up to a punch displacement of $d = 20\,\mathrm{mm}$ there is also no discernible deviation when comparing to the experimental data, despite the use of a simplified material model across all simulations. However, for larger punch displacements, these simplifications introduce discrepancies in the punch force. Notably, as the simulation model does not account for material damage, the prediction of material failure is beyond the scope of this investigation. The primary aim of

this investigation is to gauge the overall reasonableness of the simulation results, while focusing on the comparison of different finite element formulations.
Figure 6 reveals that, while the simulation results for global quantities such as punch force exhibit a high degree of similarity, a more detailed analysis, such as for example the plot of the stress in the X-direction, uncovers disparities. Specifically, Shell 16 tends to underestimate normal stress in X-direction when compared to the three-dimensional solution utilizing five solid elements across the sheet thickness. Conversely, the thick Shell 26 tends to overestimate this stress component, whereas the cubic 3D-shell closely aligns with the solid solution. However, it is important to note that these differences are relatively minor. The analysis indicates that the problem is membrane-dominated, with a high membrane stress, and bending stress plays a comparatively minor role. Consequently, cross-sectional warping is minimal, and stress in transverse direction is also relatively small. As a result, there are almost no discernible distinctions in the results of the different element formulations for other quantities of interest.

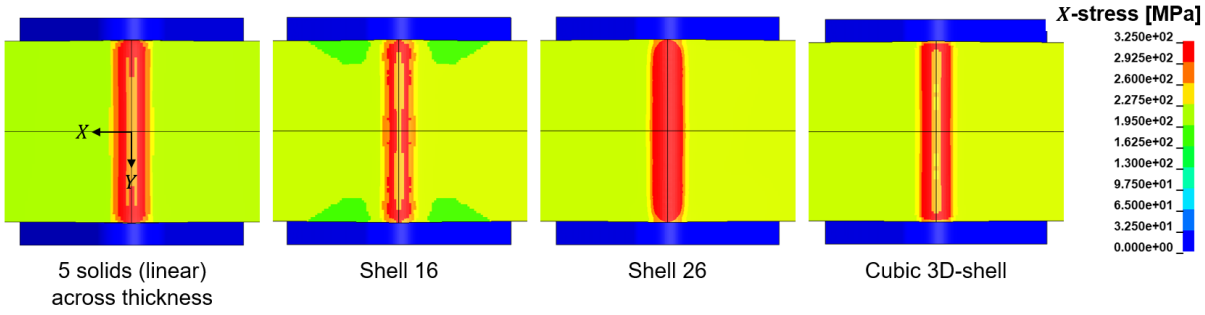

Fig.6: Normal stress in X-direction below the punch at $d = 20\ mm$ for different element formulations.

3.3 Deep drawn generic car body part

To demonstrate the viability of higher-order 3D-shell elements for industrial problems, a deep drawing process of a generic car body part based on the BMW test model RWU-80 is considered next. The test model was designed by Katy Hammer from BMW Group, further details are given in Fleischer et al. [8]. This test model represents typical geometries of real deep drawing components without corresponding to a specific component. The blank with a thickness of $T = 1.16\ \mathrm{mm}$ is meshed with about 50 000 shell elements and the explicit simulations are performed under conditions close to the industrial setup. In order to compare standard shell elements and higher-order 3D-shell elements, a simple material model (***MAT024**) is used that can be applied to both element formulations. The necessary data for the material card of an AA6014-T4 aluminum alloy were provided by Fraunhofer IWM. The objective of the simulation is to verify that the higher-order 3D-shell element is applicable in simulations on an industrial scale. Regarding this, the simulation results show that the cubic 3D-shell element can reproduce the results of the standard shell element (Shell 16). As an example, Figure 7 shows the results for the effective plastic strain after the forming process for both element types. This example successfully demonstrated that the higher-order 3D-shell elements are applicable for industrial scale simulations.

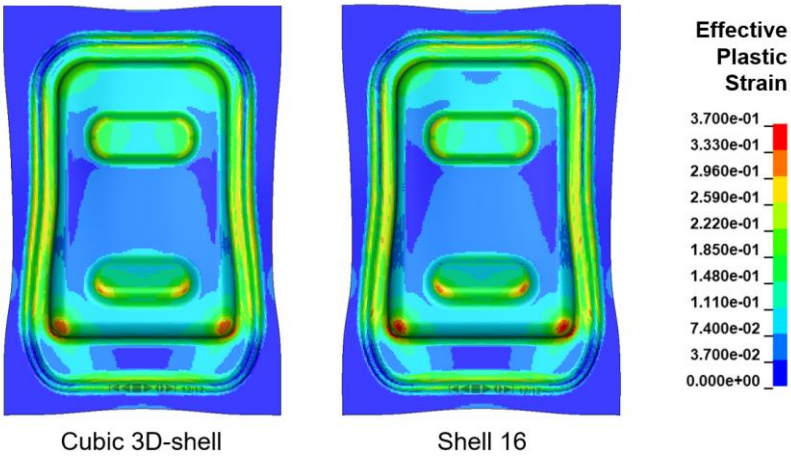

Fig.7: Effective plastic strain after the forming process for test model RWU-80 from [8].

In addition to demonstrating the applicability of the higher-order 3D-shell elements, the effect of plastic anisotropy with respect to the in-plane and out-of-plane behavior on sheet metal forming simulations was also analyzed in more detail on this model. For this analysis, we refer to Part II of this contribution [9].

4 Efficient utilization of higher-order 3D-shell elements

A significant concern in applying three-dimensional sheet metal forming simulations in industry is computational efficiency. This section examines three aspects related to this issue in the context of prospective application of higher-order 3D-shell elements. Firstly, it looks into deciding in which models or model regions to use higher-order 3D-shell elements. This results in a general guideline for the users, allowing them to use those elements only when necessary. Secondly, the study explores the necessity for finer meshes due to the extended out-of-plane kinematics of the higher-order 3D-shell element. This is investigated by examining the influence of the element size on the deviation from the reference solution. Lastly, a comparison of computational efficiency covering the higher-order 3D-shell elements and standard LS-DYNA elements (shells and solids) is conducted.

4.1 Development of a modeling guideline

Our objective is to facilitate the effective application of the higher-order 3D-shell element. This study aims to establish an initial practical guideline for its usage, employing a simple criterion that can be checked a-priori to a simulation. This offers dual benefits. First, it advocates utilizing the higher-order 3D-shell element instead of standard shell elements solely when it is necessary. Second, it allows for the implementation of mixed meshes, meaning restricting the use of the higher-order 3D-shell element to critical model areas only. Other model regions can be meshed with standard shell elements and the two element types could be coupled at their interface, as depicted in Figure 8. This strategy would increase computational efficiency by reducing the number of degrees of freedom.

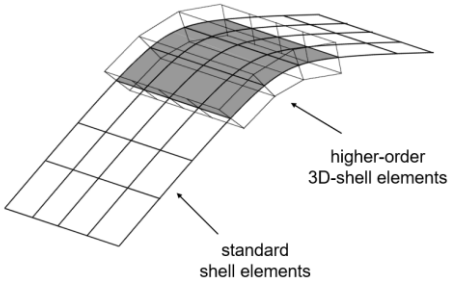

Fig.8: Mixed mesh with standard shell elements in regions of small curvature and higher-order 3D-shell elements in regions of large curvature.

We identify those critical regions and situations through an analysis of the influence of the higher-order deformation modes of the cubic 3D-shell element on the strain – see Figure 1 (quadratic and cubic deformations of cross-sectional fibers). For this we study the bending of a sheet metal strip of length l and thickness t by displacement of the supports, as shown in Figure 9. In Y-direction one element is used and the plane strain condition is enforced. In this benchmark, the support on the right in the figure is moved in negative X-direction, which continuously decreases the bending radius $R = [10\,000, 145]\,\mathrm{mm}$ of the sheet. This problem is investigated for five different sheet thicknesses $T = \{100, 50, 20, 10, 5\}\,\mathrm{mm}$. For each simulation a mesh of 20 higher-order 3D-shell elements with nine Gauss points in sheet-thickness direction and an elasto-plastic material model (`*MAT024`, steel grade DD14) is used.

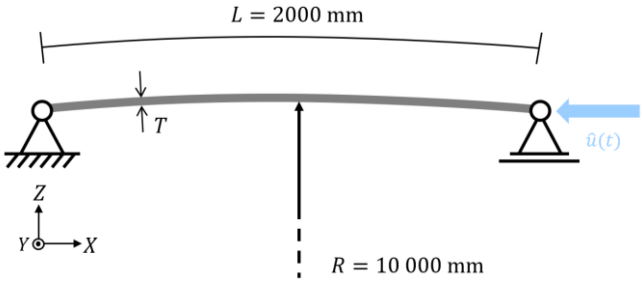

Fig.9: Problem description of the displacement-controlled bending test of a sheet metal strip.

In Figure 10, the strain is evaluated for a sheet thickness of $T = 50\,\mathrm{mm}$ and a bending radius of $R = 150\,\mathrm{mm}$. In the shell element highlighted in black, the strain in the element x-direction is calculated at each Gauss point across the element thickness coordinate z, once considering the higher-order degrees of freedom for the strain calculation (represented by the black line in Figure 10, left) and once neglecting those degrees of freedom (blue line). Both strain calculations stem from the same simulation and are done in parallel, therefore the geometry is the same for both. Figure 10 shows a clear deviation

in the element-local x-strain if the higher-order degrees of freedom are neglected, especially at the top and bottom surface of the higher-order shell element. Using the difference of strain at each Gauss point i, an error e_i can be calculated as follows

$$e_i = \frac{\left|\varepsilon_i^{wHO} - \varepsilon_i^{woHo}\right|}{\left|\varepsilon_i^{wHO}\right|}, \quad \mathrm{i} = 1 \ldots 9, \tag{7}$$

which is as large as 10.0% for the bottom Gauss point.

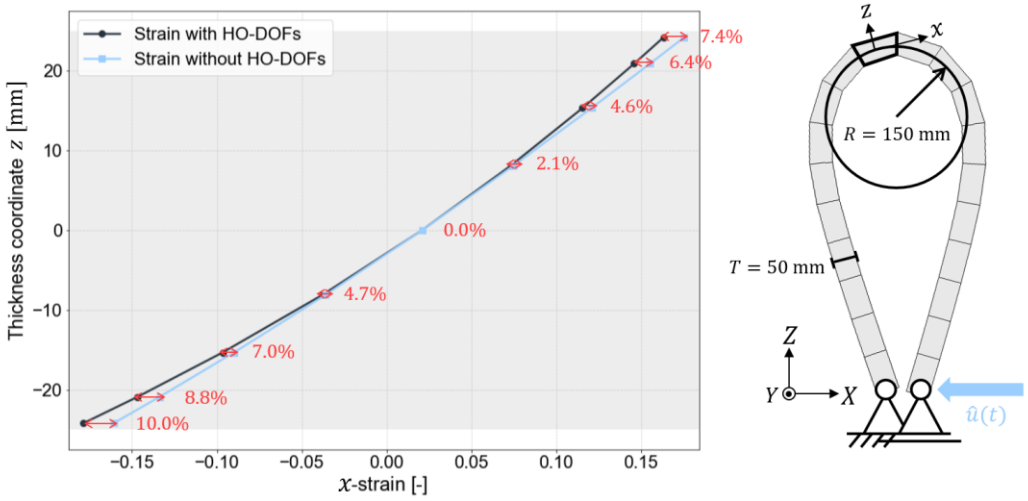

Fig.10: Strain calculated with and without higher-order deformations in local x-direction of the shell element marked in black.

The maximum of the difference in strain at each Gauss point i is evaluated for all examined sheet thicknesses and within the chosen bending radius interval. Here, the normalization is performed with respect to the maximum strain of all Gauss points over the complete simulation instead of the maximum strain for each specific bending radius. This leads to the following calculation of the maximum error:

$$e_{\max}(r,h) = \frac{\max\left|\varepsilon_i^{wHO}(r,h) - \varepsilon_i^{woHo}(r,h)\right|}{\max\left|\varepsilon^{wHO}(h)\right|}, \quad \mathrm{i} = 1 \ldots 9. \tag{8}$$

Furthermore, we introduce the ratio of the bending radius R to the square root of the sheet thickness T. In the following, this ratio is denoted by β:

$$\beta = \frac{R}{\sqrt{T}}. \tag{9}$$

This results in the plot of the maximum error in the element-local x-strain relative to the maximum local x-strain for each sheet thickness T against the ratio β in Figure 11.

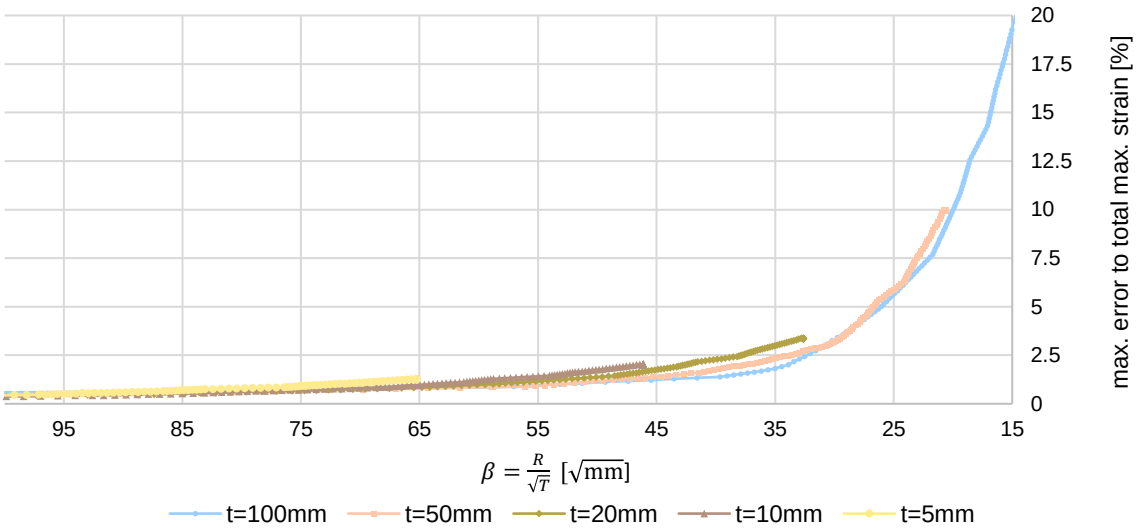

Fig.11: Maximum error of strain relative to maximum strain when neglecting the higher-order degrees of freedom in its calculation against ratio β.

It can be observed that the maximum error increases exponentially for small bending radii and large sheet thicknesses. When plotted against the ratio β, all error curves closely align, which allows the derivation of a first general rule for the application of the cubic 3D-shell element. For example, if a maximum error of 2% is tolerated with respect to the maximum strain, a cubic 3D-shell element should be used for sheet metal forming simulations in which a ratio β smaller than 45 occurs. From this, the position of the coupling between standard shell elements and higher-order 3D-shell elements can also be derived. The interface between the elements should be located in regions of the model where β is greater than 45.

4.2 Influence of element size

This study explores the necessity for finer meshes due to the extended out-of-plane kinematics of the higher-order 3D-shell element. It is a general phenomenon that increasing model fidelity – here the higher-order kinematics in transverse direction – demands finer in-plane meshing to fully utilize the benefits of the improved approximation. To investigate the influence of the element size, a bending test is studied, which is shown in Figure 12 (left). A straight sheet of length $L = 60\,\mathrm{mm}$ and thickness $T = 1.50\,\mathrm{mm}$ with an elasto-plastic material (***MAT024**) is investigated. In Y-direction, one element is used and plane strain conditions are applied. In X-direction, the sheet is meshed with shell elements with edge length $h = 1.00\,\mathrm{mm}$ in the outer, light gray regions. In the middle, dark gray region, the element edge length is varied in subsequent investigations ($h = \{1.00, 0.50, 0.25\}\,\mathrm{mm}$). A mesh with an element edge length of $h = 0.125\,\mathrm{mm}$ is used to obtain a reference solution for each element formulation in the following. The simulations are evaluated up to the point where a bending radius of $R = 1.50\,\mathrm{mm}$ is reached. The final deformed configuration is shown in Figure 12 (right).

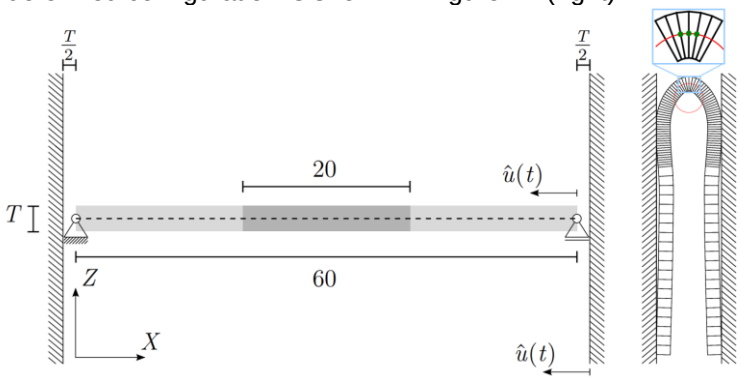

Fig.12: Problem description of the bending test (left) and final deformed configuration (right).

In the following, the influence of the element size on the quality of the results is investigated for three element formulations. Shell 2 is used as a reference. This is compared with the linear 3D-shell element and the quadratic 3D-shell element. In the following, the absolute deviations of the different element formulations from the respective reference solution are compared:

$$\Delta\varepsilon_{\mathrm{pl}}^{\text{Shell 2}} = \varepsilon_{\mathrm{pl}}^{\text{Shell 2}} - \varepsilon_{\mathrm{pl}}^{\text{ref, Shell 2}}, \tag{10}$$

$$\Delta\varepsilon_{\mathrm{pl}}^{\text{Lin. 3D-Shell}} = \varepsilon_{\mathrm{pl}}^{\text{Lin. 3D-Shell}} - \varepsilon_{\mathrm{pl}}^{\text{ref, Lin. 3D-Shell}}, \tag{11}$$

$$\Delta\varepsilon_{\mathrm{pl}}^{\text{Quadr. 3D-Shell}} = \varepsilon_{\mathrm{pl}}^{\text{Quadr. 3D-Shell}} - \varepsilon_{\mathrm{pl}}^{\text{ref, Quadr. 3D-Shell}}. \tag{12}$$

Figure 13 shows this deviation as an example for a sheet thickness $T = 1.50\,\mathrm{mm}$ and an element edge length $h = 0.50\,\mathrm{mm}$ for all three element formulations. The deviation from the reference solution for the linear 3D-shell element is of the same order of magnitude as for Shell 2. Accordingly, finer meshing is not necessary for the linear 3D-shell element compared with Shell 2, the same meshing as previously used for the standard shell can be used for this element formulation. In contrast, there is a greater deviation from its reference solution for the quadratic 3D-shell element. There, the difference to its reference solution is by about a factor of three higher. Thus, finer meshing can be useful for the quadratic 3D-shell element compared to Shell 2 in order to fully exploit the improved approximation in sheet-thickness direction.
The reason for this larger deviation from the reference solution for the quadratic 3D-shell element is a dependence of the thickness strain on the mesh density. Figure 14 shows the final state of the bending test for two different element sizes of the quadratic 3D-shell element. In the upper part of the figure, the two meshing variants are shown. In the lower part of Figure 14, the element deformations of the coarse and fine mesh are compared. It is visible that for the quadratic 3D-shell element, the strain in the

transverse direction is underestimated for a coarse mesh. In addition, deviations occur in the strain distribution across the thickness (Figure 14, bottom right). Not shown is the overestimation of cross-sectional curvature that occurs in this case for coarse meshes. The results of this study can be applied to the cubic 3D-shell element, since the cubic 3D-shell element contains the deformations of the quadratic 3D-shell element because of its hierarchic formulation. Consequently, finer meshing compared to Shell 2 may also be useful for the cubic 3D-shell element.

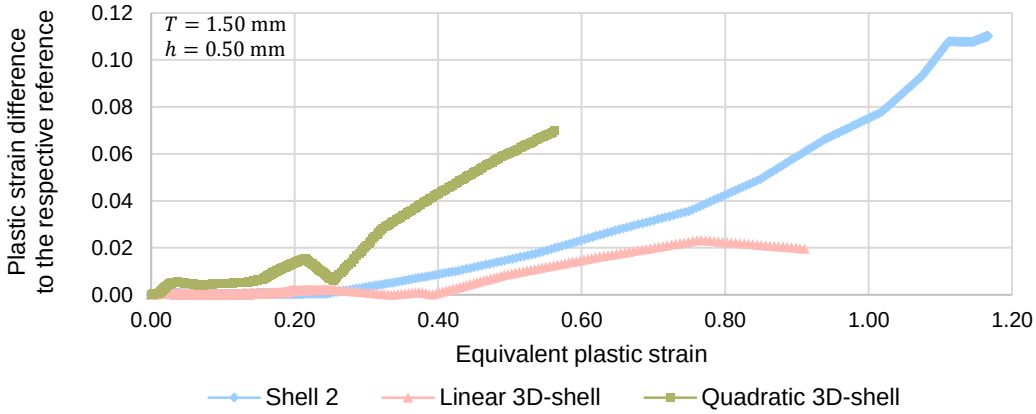

Fig.13: Error in the plastic equivalent strain for the linear and quadratic 3D-shell element in comparison to Shell 2 for a fixed mesh density.

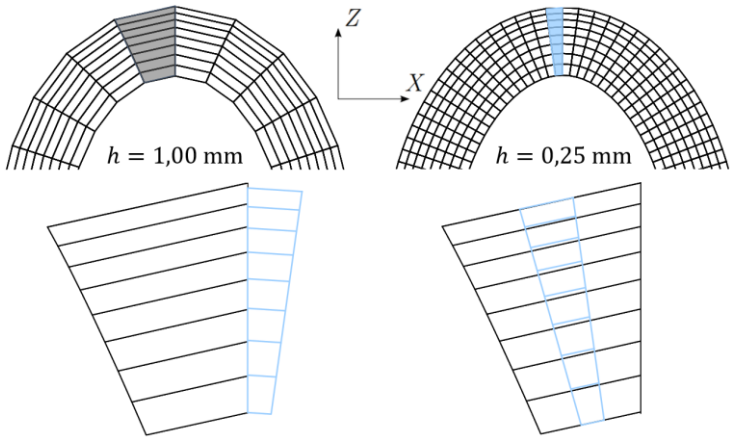

Fig.14: Comparison of two solutions to the bending test with different mesh densities of the quadratic 3D-shell element.

4.3 Comparison of numerical efficiency

In order to make the element suitable for industrial applications, the performance of the cubic 3D-shell element is improved by a more efficient calculation of the velocity strain given in Equation (6). In addition, 3D-shell variants with a lower number of deformation modes and a reduced computing time were implemented. To measure their performance, the computing time for 5000 time steps of a tensile test simulation with (`*MAT024`) is compared to commercially available elements. Each variant uses five integration points in transverse direction.

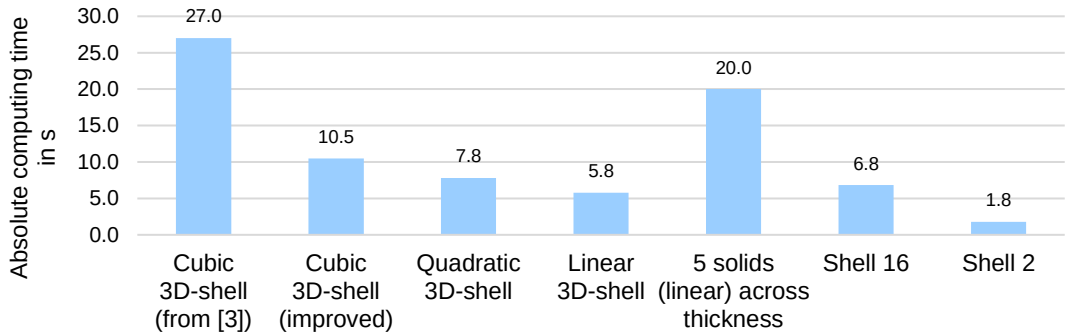

Fig.15: Comparison of computing time for 5000 time steps of a tensile test simulation.

Figure 15 shows that the computing time for the improved cubic 3D-shell element is now approximately half the computing time for five solid elements across the thickness of the tensile specimen. The 3D-shell element variants with a lower number of deformation modes are even more computationally efficient and in a range of standard shell elements. We therefore deem the computational efficiency of the higher-order 3D-shell elements suitable for large scale industrial applications.

5 Summary and outlook

The improved prediction quality of a higher order 3D-shell element for stress and strain in sheet metal forming simulations is demonstrated for practical sheet metal forming problems. Results from numerical tests indicate that the element is able to represent the behavior in critical sheet metal forming simulations better than Reissner-Mindlin shell elements, see also [3]. Simulation results with the higher-order 3D-shell element give results close to full 3D-simulations with solid elements while requiring significantly less computing time.

Studies supporting the efficient utilization of the higher-order 3D-shell element are conducted. A first modeling guideline is developed, based on the error in strain. If an error of 2% is tolerable, the higher-order 3D-shell element should be used, if the ratio β of bending radius R and square root of the sheet thickness T is smaller than 45 ($\beta = \frac{R}{\sqrt{T}} < 45$). For smaller ratios β the error in the strain increases exponentially. Studies on the element size conducted in this contribution show that for linear 3D-shell elements the same meshes can be used as for standard shell elements, resulting in a similar deviation from the respective reference solution. For quadratic and cubic 3D-shell elements a finer meshing compared to Shell 2 can be useful in order to fully exploit the improved approximation in transverse direction of these higher-order elements. Lastly, the efficiency of the higher-order 3D-shell elements is improved, achieving a computing time suitable for large scale industrial applications.

Further research can focus on giving more detailed guidelines for the efficient utilization of the higher-order 3D-shell, considering for example one-sided contact and friction, resulting in shear strain. In the future, the concept of higher-order 3D-shell elements could also be applied to other material classes, such as fiber-reinforced plastics.

6 Acknowledgement

The research projects 19707 N and 21466 N from the European Research Association for Sheet Metal Working have been funded by the Federal Ministry of Economic Affairs and Climate Action the German Federation of Industrial Research Associations (AiF) as part of the programme for promoting industrial cooperative research (IGF) on the basis of a decision by the German Bundestag. The authors would like to thank Michael Fleischer from BMW Group for providing the finite element model RWU-80 for simulating the generic car body part. They would also like to acknowledge Christoph Schmied from DYNAmore GmbH for providing help and guidance for implementing the higher-order 3D-shell element in the developer version of the commercial Finite Elements Software LS-DYNA.

7 Literature

[1] Fleischer, M.: „Absicherung der virtuellen Prozesskette für Folgeoperationen in der Umformtechnik“. Thesis, Technical University of Munich, 2009.

[2] Willmann, T., Wessel, A., Beier, T., Butz, A., Bischoff, M.: “Cross-Sectional Warping in Sheet Metal Forming Simulations”, 13th European LS-DYNA Conference, 2021.

[3] Schilling, M., Willmann, T., Bischoff, M.: „3D-Shell Elements for Improved Prediction Quality in Sheet Metal Forming Simulations”, 16th LS-DYNA Forum, 2022.

[4] Bathe, K.J., Dvorkin, E.N.: “A formulation of general shell elements – The use of mixed interpolation of tensorial component”, Internat. Journal for Numerical Methods in Engineering 22, 1986

[5] Willmann, T, Bieber S., Bischoff, M.: „Investigation and Elimination of Nonlinear Poisson Stiffening in 3d and Solid Shell Finite Elements”, International Journal for Numerical Methods in Engineering, 2022.

[6] Başar, Y., Weichert, D.: „Nonlinear Continuum Mechanics of Solids”, Springer, 2000.

[7] Xinhai, Z., Zhang, L.: „Advance in Sheet Metal Forming - One-Step Solution, Multi-Beads, Gravity Prebending, Auto Nets, and Local Compensation”, 12th Internat. LS-DYNA Users Conf., 2012.

[8] Fleischer, M.; Sitz, S.; Asen, F.; Craighero, P.; Paramasivam, N.: “Simulation of Sheet Metal Forming – Current Developments”, 16. LS-DYNA Forum, 2022.

[9] Wessel, A., Butz, A., Schilling, M., Willmann, T., Bischoff, M.: „ Higher-Order 3D-Shell Elements and Anisotropic 3D Yield Functions for Improved Sheet Metal Forming Simulations: Part II”, 14th European LS-DYNA Conference, 2023.